Dual-energy CT spectra optimization for proton treatment planning

Gloria Vilches-Freixas, Jean Michel Létang, Nicolas Ducros and Simon Rit

***Abstract*—The purpose of this study was to determine the optimal dual-energy spectra for the treatment planning of proton therapy. We have evaluated the effect of various voltages and tin filtration combinations on the relative electron density (RED) map accuracy and precision. The RED is directly related to the stopping-power (SP) map and thus to the accuracy of the proton range estimation. An acquisition setup representing a medium-size body irradiation was evaluated. For all spectra combinations, virtual CT projections of the Gammex 467 tissue characterization phantom were simulated with realistic energy-integrating detector response model. Two situations were simulated: an ideal case without noise (infinite dose) and a realistic situation with a Poisson noise corresponding to a 20 mGy central dose. To derive the RED maps from dual-energy imaging, the projection-based basis material decomposition method proposed by Alvarez and Macovski (1976) was implemented. It was observed that the energy separation between the incident spectra had little influence on the RED accuracy but a strong influence on the precision. Different optimal ranges of low and high energy tube voltages and additional tin thicknesses that maximize the overall accuracy and the precision of RED maps were found. However, when studying each phantom material separately, a large variability of the optimal spectra was observed. An emphasis on the materials present in the anatomical region of interest must be made during the optimization process of the dual-energy spectra.**

I. Introduction

Dual energy computed tomography (DECT) imaging consists in recording two sets of acquisitions of an object at different X-ray voltages. By combining these images, either in the projection domain (prior to image reconstruction) or in the image domain (after image reconstruction), one can characterize the patient tissues. Relative electron density (RED) and effective atomic number (Z_{eff}) are quantities commonly used for material segmentation in radiotherapy applications that can be estimated from DECT. In the proton therapy context, the range of protons in patients is determined from the stopping power ratio (SPR) of tissues relative to water along the beam path. SPR can be derived from RED and Z_{eff} maps and the Bethe-Bloch equation [1], or by establishing a polyline curve (RED, SPR/RED) through calibration [2]. There are different commercial strategies to perform DECT such as dual-source, fast kV-switching and dual-layer scanners. For all techniques, the choice of the low energy (LE) and the high energy (HE) spectra influences the imaging output. The performance of dual-energy imaging is commonly evaluated in terms of contrast-to-noise ratio (CNR) or signal-to-noise ratio (SNR). In this work, we focus on finding an optimal combination of voltages and source filtration to maximize the figure of merit specific to proton therapy dose calculations: the accuracy and the precision of the extracted RED maps.

Université de Lyon, CREATIS, CNRS UMR5220, Inserm U1206, INSA-Lyon, Université Lyon 1, Centre Léon Bérard, Lyon, France (e-mail: simon.rit@creatis.insa-lyon.fr).

II. Materials and Methods

A. Phantom

The 33-cm diameter Gammex RMI 467 (Gammex, Middleton, WI) tissue characterization phantom was used to represent a medium-size body. Sixteen inserts mimicking human tissue attenuation properties positioned as described in Figure 1 with mass densities ranging from 0.3 to 1.82 g/cm^3 and known chemical compositions were considered. The index-to-material mapping and the reference RED values are provided in Figure 1. For each insert, the electron density relative to water was estimated by:

$$RED_m = \frac{\rho_m \sum_i \omega_i \left(\frac{Z}{A}\right)_i}{\rho_{\mathrm{W}} \left(\frac{Z}{A}\right)_{\mathrm{W}}} \quad (1)$$

where the index m refers to the insert material and the label W to water. ρ is the mass density, ω_i is the fraction by weight of the i^{th} element and Z/A is the ratio of number of electrons per molecular weight.

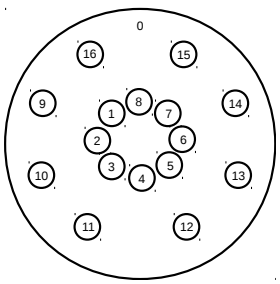

ID	Materials	RED
0	Water	1.000
1	CB2-50% $CaCO_3$	1.470
2	BR12 Breast	0.957
3	SB3 Cortical Bone	1.693
4, 15	AP6 Adipose	0.922
5, 14	LV1 Liver	1.069
6	BRN-SR2 Brain	1.046
7, 12	Water Solid	0.990
8, 9	LN300 Lungs	0.292
10	LN450 Lungs	0.438
11	CB2-30% $CaCO_3$	1.285
13	IB3 Inner Bone	1.092
16	B200 Bone Mineral	1.102

Fig. 1: Left: Gammex 467 phantom. Right: Insert ID, material name and reference RED values.

B. X-ray spectra

SpekCalc [3] was used to generate the X-ray spectra from 60 kV to 140 kV with 2 kV steps, 10° anode angle, 2.5 mm Al (required minimum filtration according to the NCRPM [4]) and 1000 mm air filtration. Each spectrum was filtered with tin (Sn) thicknesses [5] ranging from 0 to 2.5 mm at 0.1 mm

increments. For the LE acquisitions, the tube voltage was varied from 60 kV to 90 kV, whereas for the HE acquisitions it was varied from 80 kV to 140 kV. No tin filtration was considered for the LE acquisitions, only the 2.5 mm Al inherent filtration to maximize the energy gap.

C. Image simulation

Combining voltages and tin thicknesses, a total of 12896 sets of CT projection data were simulated with and without noise. Virtual CT acquisitions of the Imaging Ring (IR) X-ray system (MedPhoton, Salzburg, Austria) were carried out by means of deterministic simulations in Gate [6] with realistic energy-integrating detector response model. Scatter-free fan-beam of 807 pixels of 1 mm acquired with 360 projections were considered. The source-to-center distance was 626 mm and the source-to-detector distance was 1026 mm. For the realistic scenario, realistic Poisson noise was applied to the projections to deliver a central dose of 10 mGy with each voltage and filtration combination, and thus a total central dose of 20 mGy with the dual-energy acquisition. In a previous work [7], we observed that the dose balance between energy levels was not critical for material decomposition with dual-energy imaging. For this reason, the same dose at the center was considered for the low and the high energy acquisitions.

1) Detector response: The detector response was generated using Monte Carlo simulations. The flat panel detector of the IR was modeled in Gate as a stack of layers of different material according to the manufacturer's description. The response of the detector was obtained by measuring the energy deposit in the scintillator layer with monoenergetic pencil beams of energies ranging from 1 to 140 keV [8]. The energy-dependent detector response used in this study is shown in Figure 2 .

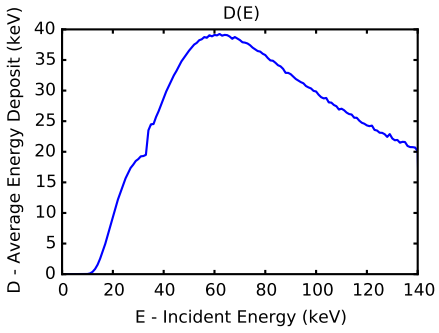

Fig. 2: Energy-dependent detector response.

2) Dose - Number of photons: For each imaging setup the number of primaries per simulation, N_{prim}, required to deliver a central dose, D_c, of 10 mGy was determined analytically assuming an homogeneous water medium:

$$N_{prim} = \frac{D_c \; A_{beam}}{\int_E S(E) \; e^{-\mu_{\mathrm{W}}(E) \; R} \; \left(\frac{\mu_{en}(E)}{\rho}\right)_{\mathrm{W}} \; E \; \mathrm{d}E} \tag{2}$$

where A_{beam} is the area covered by the beam at the isocenter, S is the energy-dependent incident spectrum, $(\mu_{en}/\rho)_{\mathrm{W}}$ and μ_{W} are the energy-dependent mass energy absorption coefficient and the linear attenuation coefficient of water taken from the NIST database [9], and R is the radius of the phantom.

3) Energy gap: For each X-ray spectra pair the incident energy gap, ΔE, was calculated as the separation between the average energies of the incident spectra:

$$\Delta E = \int_0^{E_2} S(E) \; E \; \mathrm{d}E - \int_0^{E_1} S(E) \; E \; \mathrm{d}E \tag{3}$$

where E_1 and E_2 are the maximum energies of the LE and the HE spectra, respectively.

D. Decomposition method

The two-material decomposition method proposed by Alvarez and Macovski (1976) [10] was implemented in the projection domain. The key idea is that the attenuation coefficient of the scanned object, $\mu(\boldsymbol{x}, E)$, can be expressed as a linear combination of two energy-dependent basis functions of two materials with energy-independent coefficients. Water (W) and compact bone (B) were chosen as basis materials. Their respective energy-dependent mass attenuation coefficients, (μ/ρ), were the basis functions and their mass densities, ρ, the coefficients:

$$\mu(\boldsymbol{x}, E) = \rho_{\mathrm{W}}(\boldsymbol{x}) \; \left(\frac{\mu}{\rho}\right)_{\mathrm{W}}(E) + \rho_{\mathrm{B}}(\boldsymbol{x}) \; \left(\frac{\mu}{\rho}\right)_{\mathrm{B}}(E) \tag{4}$$

Two sinograms of the same object are available in DECT by performing an acquisition with LE and HE spectra. A system of two equations can then be determined for each projection angle:

$$I_{\mathrm{LE}}(\rho_{\mathrm{W}}, \rho_{\mathrm{B}}) = \int_E S_{\mathrm{LE}}(E) \; D(E) \exp\left(-\int_L \mu(\boldsymbol{x}_l) \; \mathrm{d}l\right) \mathrm{d}E \tag{5}$$

$$I_{\mathrm{HE}}(\rho_{\mathrm{W}}, \rho_{\mathrm{B}}) = \int_E S_{\mathrm{HE}}(E) \; D(E) \exp\left(-\int_L \mu(\boldsymbol{x}_l) \; \mathrm{d}l\right) \mathrm{d}E \tag{6}$$

where L is the line-segment between the source and a detector pixel, I_{LE} and I_{HE} are the measured intensities, S_{LE} and S_{HE} are the weights of the polychromatic photon spectra, and $D(E)$ the detector response. Instead of solving this system numerically, the unknowns can be obtained by direct approximation with a power series of the logarithm of I_{LE} and I_{HE} [11] through a calibration procedure. A fourth degree polynomial with twelve terms was used to solve this system of equations. Image reconstructions of water and compact bone mass densities were performed using filtered backprojection on a 380×380×1 grid with 1×1×1 mm^3 voxels size, i.e., in the central slice only. On a pixel-by-pixel basis, the RED image was derived from the total mass density image ρ and Equation 1:

$$\rho(\boldsymbol{x}) = \rho_{\mathrm{W}}(\boldsymbol{x}) + \rho_{\mathrm{B}}(\boldsymbol{x}) \tag{7}$$

$$\left(\frac{Z}{A}\right) = \frac{\rho_{\mathrm{W}}}{\rho} \; \left(\frac{Z}{A}\right)_{\mathrm{W}} + \frac{\rho_{\mathrm{B}}}{\rho} \; \left(\frac{Z}{A}\right)_{\mathrm{B}} \tag{8}$$

E. Figures of merit

For each (LE, HE, mm Sn) tuple, the estimated RED image was compared to the ground-truth values. The relative accuracy and precision were calculated in a region-of-interest (ROI) of 3/4 the size of the insert. The absolute accuracy and the precision of the RED averaged over all inserts were also computed. First, the reconstructed RED images without noise were used to determine the optimal voltages and filtration that maximizes the overall accuracy. Then, the RED images acquired in a realistic imaging setup, in the presence of noise, were investigated. Finally, the optimal energy spectra for a representative tissue of each insert group was studied separately.

III. Results and Discussion

For both the ideal and the realistic situations, a relative electron density image per (LE, HE, mm Sn) tuple was obtained after decomposition and reconstruction. In total, 12896 tuples were investigated. The reconstructed RED images were compared to the ground-truth values and, for each image, the following quantities were extracted: accuracy and precision averaged over the sixteen phantom inserts, and accuracy and precision for each phantom insert separately. From among these data, a tuple of values that maximizes the overall accuracy was selected: (78 kV LE, 94 kV HE, 0.1 mm Sn). From this point, a sensitivity analysis of the accuracy and the precision as a function of the low voltage, the high voltage and the additional filtration was done. Orthogonal slices for both the ideal scenario and the noisy situation are shown in Figure 3. The last row of Figure 3, which corresponds to the overall precision of the realistic situation, shows that the worst precision is achieved at those ranges where the accuracy is maximized.

For the realistic scenario, the overall accuracy and precision were plotted against the incident energy gap, as shown in Figure 4. The overall accuracy was not strongly dependent on the spectra separation, whereas the overall precision asymptotically approached a 4.7% level with increasing energy gap. This level of precision was achieved from an energy gap of 60 keV. A zero precision was expected for the simulations without noise. Nevertheless, due to the voxelized phantom geometry with a sub-optimal resolution, interpolation errors of the 3D reconstruction process affected the overall precision. A constant value of 2.6% was estimated for all RED images without noise which is included in the noisy simulations of Figure 3 and 4.

The SPR map estimated from the RED image would then be used to compute the proton range in the patient. Even though the presence of noise in the SPR image is a concern, the noise is likely to be averaged along the voxels of the beam path and, thus, the final impact on the proton range should not be dramatic. On the other hand, accuracy errors will add up along the beam path and the error in the range will be more significant. For this reason, maximizing the accuracy seems more appropriate. Moreover, the 20 mGy central dose value considered in this study is very low and, increasing the imaging dose would improve the precision.

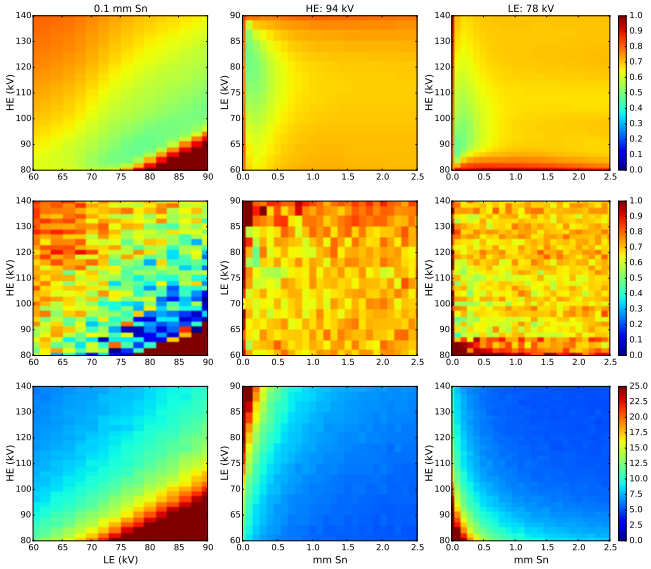

Fig. 3: Overall RED accuracy and precision as a function of the LE, HE and tin filtration. From top to bottom: overall accuracy for the ideal situation (no noise), overall accuracy (middle) and overall precision (bottom) for the realistic acquisition. From left to right: LE-HE plot at 0.1 mm Sn, LE-mm Sn plot at HE: 94 kV, HE-mm Sn plot at LE: 78 kV. Colorbars indicate the percentage error and the relative uncertainty for the accuracy and the precision, respectively.

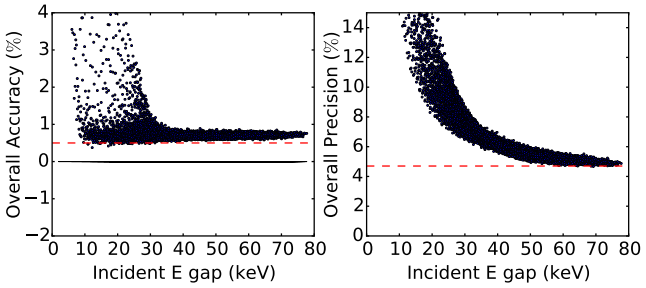

Fig. 4: Overall RED accuracy and precision as a function of the incident energy gap for the realistic acquisition scenario. Dashed red lines indicate the 0.5% accuracy level (left) and the 4.7% precision level (right).

Another approach to reduce image noise is to make use of regularized reconstruction algorithms instead of filtered backprojection for image reconstruction.

The accuracy and the precision of each phantom insert relative to the (78 kV LE, 94 kV HE, 0.1 mm Sn) tuple are shown in Figure 5. Low density tissues (lungs LN300 and LN450) show the worst precision. In terms of accuracy, all inserts fall within the $\pm 1\%$ error range.

Then, we studied whether the optimal spectra determined in terms of the overall accuracy corresponded to the optimal spectra for each insert group. One representative insert per tissue group was selected: LN450(10) for the low (RED$<$0.5), AP6(15) for the medium (0.5$<$RED$<$1.2) and CB2-50(1) for the high (RED$>$1.2) density. From the (78 kV LE, 94 kV HE,

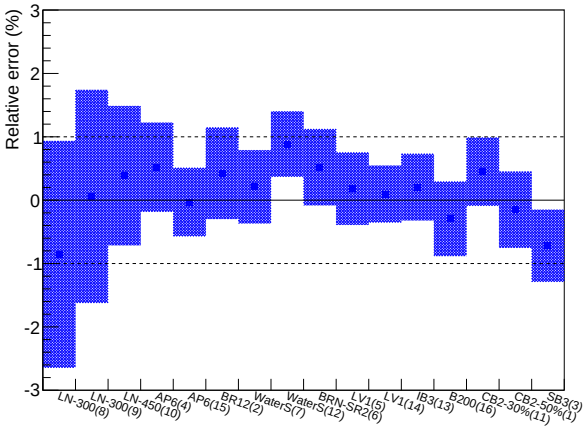

Fig. 5: RED accuracy and precision results for each insert of the Gammex 467 phantom (78 kV, 94 kV, 0.1 mm Sn) for the 20 mGy acquisition.

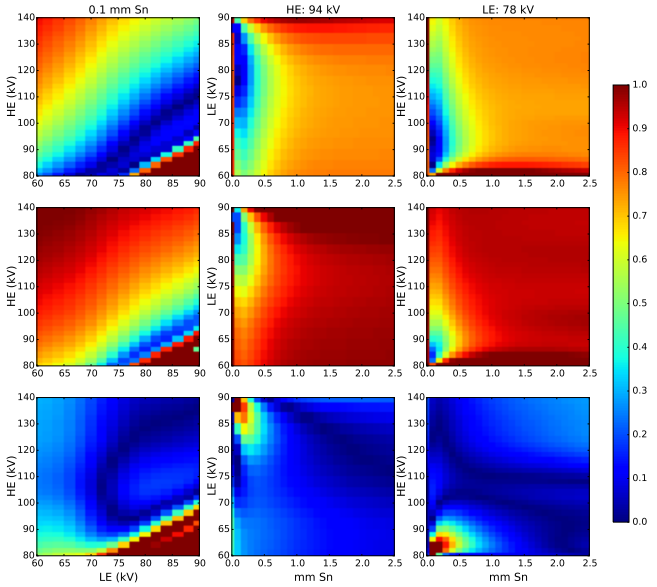

Fig. 6: From top to bottom, RED accuracy results as a function of the LE, HE and tin filtration for the insert: LN450, AP6 and CB2-50. From left to right: LE-HE plot at 0.1 mm Sn, LE-mm Sn plot at HE: 94 kV, HE-mm Sn plot at LE: 78 kV. The colorbar indicates the percentage error for the accuracy. Data corresponding to the ideal situation, without noise.

0.1 mm Sn) point, orthogonal slices were plot to study the dependence of the inserts accuracy with the low voltage, the high voltage and the additional filtration. Due to the limited space, only those plots relative to the ideal situation are shown in Figure 6. However, these plots mask the increased presence of noise in the low density inserts. Low and medium density inserts are more sensitive to the energy spectra than high density inserts. The optimal spectra selected by means of the overall accuracy seems adequate for low and medium density inserts. According to these plots, for high density tissues it is preferable to have high LE, medium HE and high filtration.

IV. Conclusion

An extensive study of the impact of the dual-energy spectra on the relative electron density accuracy and precision was done. An ideal situation without noise and a realistic acquisition with a total dose of 20 mGy were considered. The optimal range of low and high energy tube voltages and additional tin thicknesses in terms of accuracy and precision were not the same. The precision was improved with increasing energy separation between the incident spectra, whereas the accuracy showed little dependence. According to these results, a material selective spectra optimization is advisable when performing dual-energy imaging of different human regions for proton treatment planning. Moreover, it would be interesting to reproduce the same study considering a large-size patient.

Acknowledgment

This work was partially supported by grant ANR-13-IS03-0002-01 (DEXTER project) from the French National Research Agency (ANR). This work was performed within the framework of the LABEX PRIMES (ANR-11-LABX-0063) of Université de Lyon, within the program "Investissements d'Avenir" (ANR-11-IDEX-0007) operated by the ANR.

References

[1] M. Yang, G. Virshup, J. Clayton, X. R. Zhu, R. Mohan, and L. Dong, "Theoretical variance analysis of single- and dual-energy computed tomography methods for calculating proton stopping power ratios of biological tissues." *Phys. Med. Biol.*, vol. 55, no. 5, pp. 1343–1362, 2010.

[2] N. Kanematsu, T. Inaniwa, and Y. Koba, "Relationship between electron density and effective densities of body tissues for stopping, scattering, and nuclear interactions of proton and ion beams," *Med. Phys.*, vol. 39, no. 2, pp. 1016–1020, 2012.

[3] G. Poludniowski, G. Landry, F. DeBlois, P. M. Evans, and F. Verhaegen, "SpekCalc: a program to calculate photon spectra from tungsten anode x-ray tubes." *Phys. Med. Biol.*, vol. 54, no. 19, pp. N433–N438, 2009.

[4] N. C. on Radiation Protection and M. Measurements. Bethesda, "Medical x-ray, electron beam and gamma-ray protection from energies up to 50 MeV, Report No. 102."

[5] A. N. Primak, J. C. Ramirez Giraldo, X. Liu, L. Yu, and C. H. McCollough, "Improved dual-energy material discrimination for dual-source CT by means of additional spectral filtration." *Med. Phys.*, vol. 36, no. 4, pp. 1359–1369, 2009.

[6] S. Jan, G. Santin, D. Strul, S. Staelens, K. Assié, and D. Autret, "GATE: a simulation toolkit for PET and SPECT," *Phys. Med. Biol.*, vol. 49, pp. 4543–4561, 2004.

[7] G. Vilches-Freixas, J.-M. Letang, K. Presich, P. Steininger, and S. Rit, "Optimal dose balance between energy levels for material decomposition with dual-energy X-ray CT," in *Radiotherapy and Oncology, Elsevier, Vol.115, pp.S506-S507, Barcelona (Spain)*, 2015.

[8] D. A. Roberts, V. N. Hansen, A. C. Niven, M. G. Thompson, J. Seco, and P. M. Evans, "A low Z linac and flat panel imager: comparison with the conventional imaging approach." *Phys. Med. Biol.*, vol. 53, no. 22, pp. 6305–6319, 2008.

[9] J. H. Hubbel and S. M. Seltzer, "Tables of X-ray mass attenuation coefficients and mass energy-absorption coefficients. National Institute of Standards and Technology (NIST). Retrieved September 2007."

[10] R. E. Alvarez and a. Macovski, "Energy-selective reconstructions in X-ray computerized tomography." *Phys. Med. Biol.*, vol. 21, no. 5, pp. 733–744, 1976.

[11] K.-S. Chuang and H. K. Huang, "Comparison of four dual energy image decomposition methods," *Phys. Med. Biol.*, vol. 33, no. 4, p. 455, 1988.